3D Printed Graphene-Based 3000 K Probe

Zhiqiang Liang, Yonggang Yao, Bo Jiang, Xizheng Wang, Hua Xie, Miaolun Jiao, Chu Liang, Haiyu Qiao, Dylan Kline, Michael R. Zachariah, and Liangbing Hu*

High-temperature heating is ubiquitously utilized in material synthesis and manufacturing, which often features a rapid production rate due to the significantly improved kinetics. However, current technologies generally provide overall and steady-state heating, thereby limiting their applications in micro/nano-manufacturing that require selective patterning and swift heating. Herein, significantly improved control over small-scale heating is reported by utilizing 3D printed reduced-graphene-oxide (RGO) probe triggered by electrical Joule heating, which enables precise heating with high spatial (sub-millimeter scale) and temporal (milliseconds) resolutions. The block copolymer-modified aqueous-based RGO ink enabled 3D printing of high-precision structures, and a bio-inspired cellular microstructure is constructed to achieve control of the electrical conductivity and maximize structure robustness (benefit for efficient heating and operability). In particular, a thermal probe featuring a microscale tip with excellent heating capabilities (up to ≈3000 K, ultra-fast ramping rate of ≈10^5 K s^{-1}, and durations in milliseconds) is fabricated. This thermal probe is ideal for surface patterning, as it is demonstrated for the selective synthesis of patterned metal (i.e., platinum and silver) nanoparticles on nano-carbon substrates, which is not possible by traditional steady-state heating. The material construction and heating strategy can be readily extended to a range of applications requiring precise control on high-temperature heating.

1. Introduction

High temperatures are ubiquitously used for materials synthesis and manufacturing, providing not only high activation energy to drive the reaction, but also ultrafast kinetics to enable

Prof. Z. Liang, Prof. Y. Yao, Dr. B. Jiang, Dr. X. Wang, H. Xie, Dr. M. Jiao, Prof. C. Liang, H. Qiao, Prof. L. Hu
Department of Materials Science and Engineering
University of Maryland
College Park, MD 20742, USA
E-mail: binghu@umd.edu
Dr. D. Kline
Department of Chemical and Biomolecular Engineering
University of Maryland
College Park, MD 20742, USA
Dr. D. Kline, Prof. M. R. Zachariah
Department of Chemical and Environmental Engineering
University of California
Riverside, CA 92521, USA

rapid and scalable fabrication. In particular, ultra-high temperatures (>2000 K) are needed to fabricate materials that require extreme conditions, such as high-entropy-alloy nanoparticles, ceramics, and high quality carbon fibers.[1] However, current heating technologies feature bulky configurations that largely limit their spatial and temporal resolutions which are only able to offer overall and steady-state heating; these capabilities alone are not ideal for micro/nanoscale synthesis and manufacturing. For example, the conventional resistance furnace and microwave heating have limited temperatures (≈1500 K) and ramping rates (≈10–20 K min^{-1}), which are too slow for micro/nanoscale fabrication that often requires rapid heating/cooling to construct delicate nanostructures. In addition, such methods are only capable of bulk heating and cannot provide localized thermal patterning capability, which is necessary for applications that require localized metallic nanoparticle patterning (e.g., fabrication of plasmonics enhanced optoelectronics).

The conventional patterning technologies, such as atomic force microscopy lithography, are not thermally applicable at high temperatures and are largely limited by time-consuming procedure and expensive equipments.[2] Current localized heating technologies, such as thermal scanning probe lithography (t-SPL),[2b,3] despite having a high spatial resolution, are largely material or equipment dependent. In addition, their maximum sustainable heating temperature range (700–1000 °C) are limited and the processing speed is often low. Therefore, developing a high-precision high-temperature heating source with superior heating and patterning capabilities is highly desirable for thermally driven micro/nano-manufacturing, yet it remains an outstanding challenge.

Toward these aims, we report a 3D printed reduced-graphene-oxide (denoted as RGO) thermal probe triggered by electrical Joule heating that functions as a high-temperature heating source with significantly improved spatial and temporal resolutions for precise thermal patterning and nanomaterials synthesis (**Figure 1**). 3D printing provides a powerful tool to construct complex 3D structures in a broad range of sizes and structures, among which direct-ink-writing (DIW), electric-field-driven microscale 3D printing, and femtoliter ink meniscus guiding evaporation could enable microscale 3D structures.[4] For example, Zhu et al. combined their
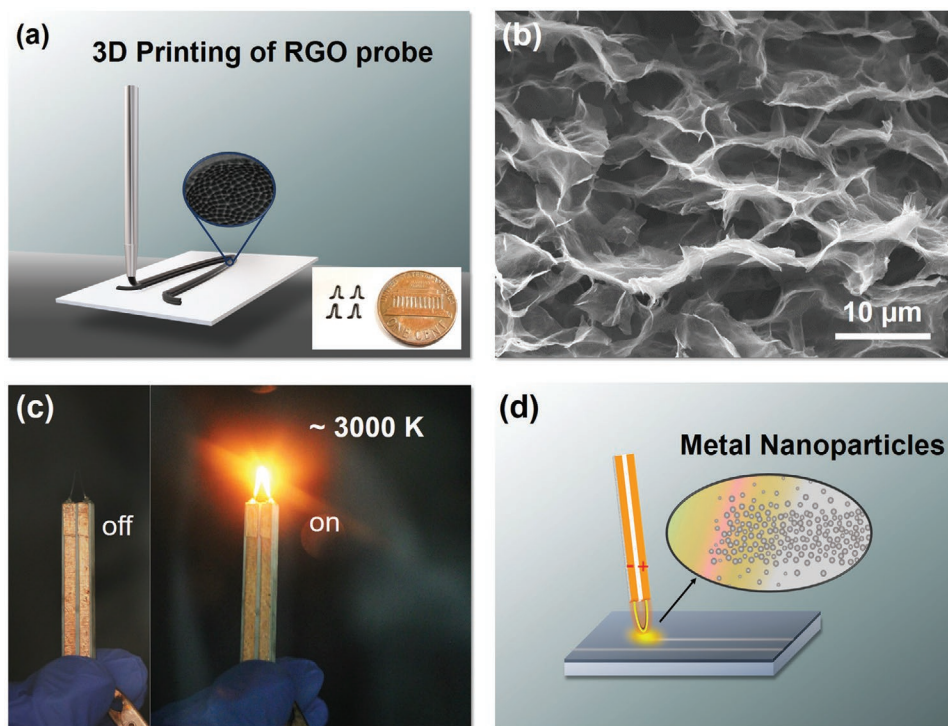
Figure 1. 3D printing of RGO probes. a) Schematic diagrams of 3D printing of RGO probe. Insets: the cellular microstructure of the RGO probe (middle) and arrays of represented as-printed RGO probes (bottom). b) Cross-sectional SEM image of the RGO probe, which shows a cellular microstructure. The cellular microstructure of the RGO probe is expected to experience a high temperature due to larger contact resistance. c) Optical image of the operation of an RGO thermal probe at "off" and "on" states (≈3000 K). The RGO thermal probe device made by fixing the probe on an alumina ceramic handle with copper electrodes. The operation of the thermal probe is performed by supplying a driving current. d) Schematic demonstration of the thermal patterning of metal NPs on the substrate through a rapid radiative heating process by the high-temperature RGO thermal probe.

electric-field-driven microscale 3D printing technology with a UV-assisted micro-transfer process to achieve rapid fabrication of micron-sized metal meshes with excellent optoelectronic properties, thus providing a promising path to address the challenge of cost-effective manufacture of metal meshes for transparent glass heaters.[4e-g] In this work, the extrusion-based DIW method was used for probe construction due to its process simplicity and good compatibility to a variety of nanomaterials. In terms of materials, RGO was chosen to print the thermal probe due to its superior flexibility for 3D printing[5] as well as excellent thermal stability with a strong C—C bond to withstand high temperatures.[6] As shown in Figure 1a, an optimized aqueous-based RGO ink with significant shearing behavior and adequate storage modulus (G') was used for the printing of the RGO probe with a tunable size, shape, and geometry. The cellular microstructure (insets in Figure 1a,b) was designed to achieve a relatively high contact resistance compared with the dense structure thereby efficient Joule heating. In addition, the strongly bonded microscopic cellular structure also has good mechanical integrity with improved operability.[7]

The printed RGO probe (after thermal reduction) was assembled on an alumina ceramic handle (Figure 1c) for electrical Joule heating operations. Figure 1c displays the operation of a representative RGO thermal probe that triggered by the input of a 500 mA driving current (i.e., Joule heating). Overall, the RGO thermal probe has excellent thermal stability and can achieve a high temperature of up to ≈3000 K, with an ultrafast

heating/cooling rate of ≈10^5 K s^{-1} and a high temporal resolution down to millisecond level. Such a thermal probe with a microscale tip feature and excellent heating capabilities put forward an effective strategy for precise thermal patterning and nanomaterial synthesis. As a demonstration, metal nanoparticles, including platinum (Pt) and silver (Ag), were rapidly synthesized on nano-carbon substrates by the RGO thermal probe and in a flexible "direct writing" process (Figure 1d), without the need for a mask or additional development steps. The high spatial (sub-millimeter) and temporal (milliseconds) resolutions, and excellent stability make this RGO thermal probe an ideal thermal source for non-equilibrium heating for material synthesizing, localized thermal treatment, and thermal-driven micro/nano-manufacturing where precise heating, in terms of both position and duration, is required.

2. Results and Discussion

Central to the extrusion-based 3D printing technique is the development of printable ink with suitable rheological properties, including significant shear thinning behavior, adequate initial storage modulus (G') and yield stress (τ_y), which in turn, depend on the solid contents, additives, and solvent.[5b,8] The ink preparation processes are briefly shown in **Figure 2**a,b, including the pre-reduction of GO suspension, the concentration of the particularly reduced GO (RGO), and the mixing of
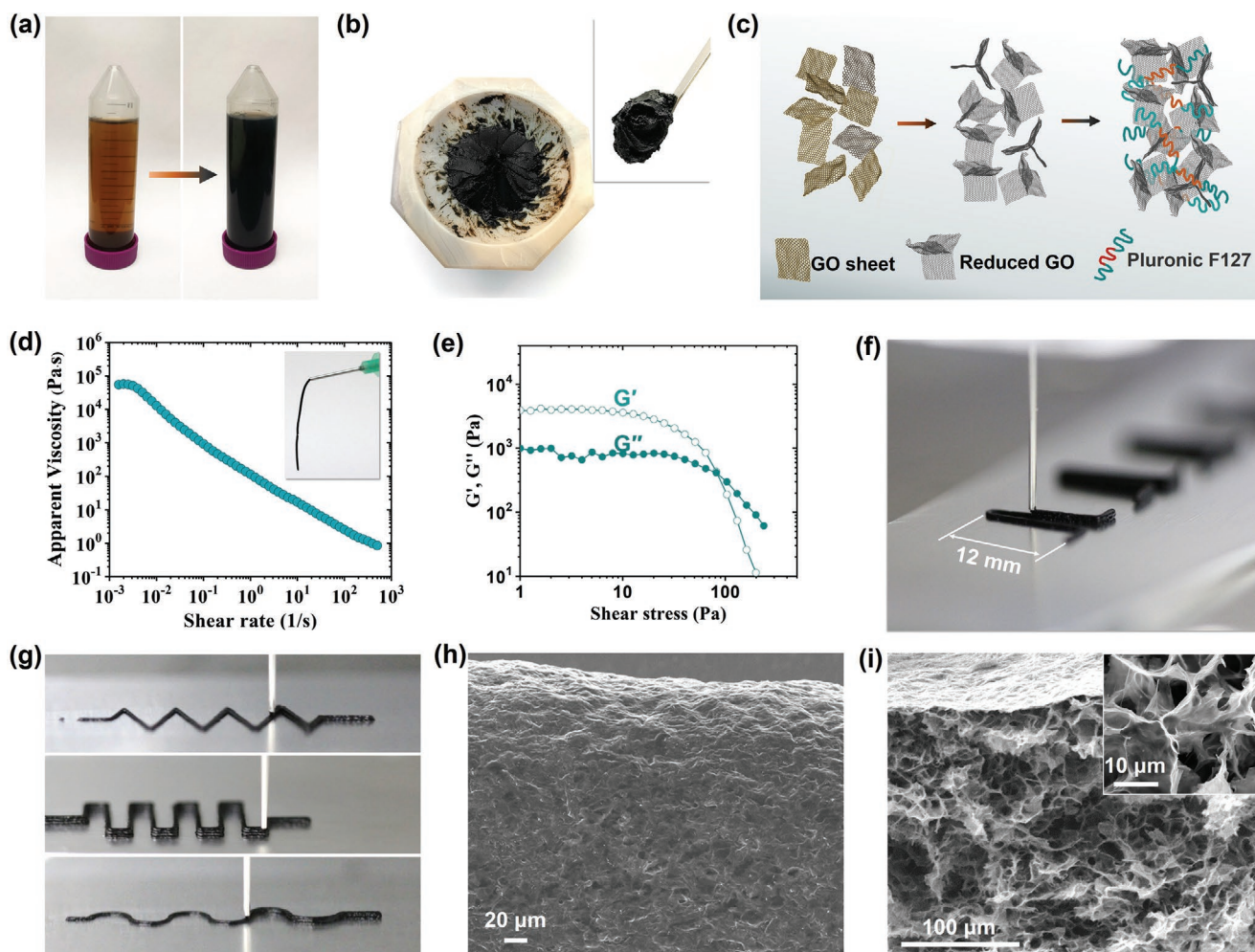
Figure 2. Ink preparation, rheological properties and 3D printed RGO probes. Optical images of the a) GO suspension and the partially reduced GO (RGO) suspension by ascorbic acid, and b) the printable RGO ink. Inset is the aqueous-based RGO ink sticked on a spoon. c) Schematic illustration of the interconnection of the GO sheets during the slow reduction process, and the interconnection between the reduced GO sheets and F127 of the printable RGO ink. d) The apparent viscosity of the RGO ink as a function of the shear rate. Inset is the ink-filament being smoothly extruded from a fine nozzle. e) Storage modulus (G') and loss (G'') modulus of the RGO ink as a function of the shear stress. f) 3D printing of RGO probes. g) 3D printing of linear RGO structures, including: saw-toothed- (top), S- (middle), and right-angle-shaped filaments (bottom) with a length of 20 mm. SEM images of h) surface and i) cross-section of the RGO probe before Joule heating.

Pluronic F–127 (see Methods in the Supporting Information for more details). The printable RGO ink (Figure 2b) features a low fluidity and self-supporting ability, as demonstrated by its lack of flow when sticked on a spoon (inset in Figure 2b). First, we synthesized large lateral-sized GO nanosheets feature a thickness of ≈0.8 nm and a lateral size ranging from ≈5 μm to several dozens of microns (Figure S1, Supporting Information) by a modified Hummers method according to previous report.[9] Compared to smaller GO nanosheets, the inks composed of GO nanosheets with larger lateral size have a higher storage modulus and shear viscosity in aqueous solution,[10] which helps to improve the printability for extrusion-based 3D printing. We partially reduced the GO suspensions using the ascorbic acid (AA) aqueous solution as a weak reductant, which allows the GO sheets to gradually grow up to partially reduced GO micro-gel structure (Figure 2c).[11] In our previous work, it has been found that the reduction degree of the GO

sheets largely affects the microstructure of the final prepared graphene structures.[7a] To obtain cellular microstructure via the freeze-casting treatment, the GO solution was partially reduced at 60 °C for 30–50 min, and the mass ratio of AA to GO was kept at 2:1. This suspension of partially reduced GO was then condensed to a high concentration printable ink using vacuum filtration. Pluronic F–127 (referred to hereafter as F127) aqueous solution (20 wt%, see Methods in the Supporting Information for more details) was used to further optimize water retention behavior as well as the stability the RGO ink (Figure 2c).[12]

We experimentally found that an aqueous-based ink with RGO concentration of ≈40 mg mL^{-1} can meet the requirements of 3D printing of the RGO probes in air without the need for any additional curing treatment during the printing process. We characterized the rheological properties of this RGO ink to investigate its printability. Figure 2d shows the apparent viscosity of this ink decreases with the increasing shear rate on a

ADVANCED
SCIENCE NEWS
www.advancedsciencenews.com

ADVANCED
FUNCTIONAL
MATERIALS
www.afm-journal.de

logarithmic scale, indicating a non-Newtonian fluid feature and a pronounced shear-thinning behavior.[5b] The shear-thinning behavior enables this ink to be extruded from the fine nozzle with diameter of 360 µm and form a stable ink-filament under adequate printing pressure (≈50–60 Psi) (inset in Figure 2d). Figure 2e displays the storage modulus (G') and the loss modulus (G'') of the RGO ink as a function of the shear stress on a logarithmic scale. The G' plateau (≈4×10^3 Pa) of the RGO ink is significantly higher than its G'' plateau (≈8×10^2 Pa), which is essential for the shape retention and self-supporting behavior of a newly printed filament during 3D printing.[5b] To further illustrate the self-supporting ability of this RGO ink, we investigated the self-supporting ability of the ink filaments across the gap (as shown in Figure S2, Supporting Information), where the freshly extruded ink filaments did not bend and sag under their own gravity even when spanning a gap as wide as 7 mm, demonstrating excellent self-supporting capability. A scaffold structure (Figure S3, Supporting Information) has also been printed to demonstrate the self-supporting capability of RGO ink and the flexible direct-ink-writing 3D printing approach. In addition to shear thinning properties and moduli, water retention is also an important issue as it affects the stability of aqueous-based ink. We found that the aqueous RGO inks without F127 tend to become sticky and clogs the nozzle of 3D printer due to the water evaporation, while the RGO inks with F127 remains stable for a longer period of time without clogging the fine nozzle.

By adjusting the printing parameters, (e.g., printing pressure/speed and nozzle diameter), we directly printed the RGO probes using this RGO ink (Figure 2f). The representative RGO probes has a line width of ≈400 µm and height of 12 mm. With this 3D printable ink, the size and shape of the RGO probe can be flexibly designed and printed by adjusting the printing parameters for meeting different heating requirements. Accordingly, we demonstrated three other kinds of structures, including saw-toothed-, S-, and right-angle-shaped filaments (Figure 2g and Figure S4: Supporting Information). In addition, we have printed smaller RGO probes with filament widths down to 100 µm (Figure S5, Supporting Information). We believe it will be possible to print micron-scale RGO probes by using the printing methods holds micron-level printing precision and optimizing RGO ink.

The as-printed RGO probes were immediately treated with liquid nitrogen to freeze the macrostructures and to create porous microstructure, followed by a freeze-drying process to remove water. Surface and cross-sectional scanning electron microscopy (SEM) images reveal the smooth surface (Figure 2h) and cellular porous internal microstructure (Figure 2i) of the 3D printed RGO probe. It has been demonstrated that the cross-linked RGO sheets in the partially reduced RGO ink can be assembled into a microscopic cellular structure via a freeze casting treatment under the extrusion of ice crystal during the freezing process.[11] The cellular microstructure makes the RGO sheets have few internal contacts and therefore a larger contact resistance, which could facilitate high-temperature Joule-heating at a low input current. Additionally, the strongly bonded cellular microstructure offers a high mechanical strength which is beneficial for its shape retention during subsequent electrical Joule heating and surface patterning operations.[7a,13]

To enable position control during electrical Joule heating, we fixed the printed RGO probe on an alumina ceramic handle and attached the probe to copper electrodes by silver paste (**Figure 3**a). This configuration could be used for manually heating specific positions or combined with automation to enable programmatically controlled localized heating. Optical images reveal that the thickness, tip width, and height of this particular RGO probe are around 0.4, 1.5, and 12 mm, respectively (Figure 3b). SEM images further characterized the small scale of this representative probe with a filament width of ≈400 µm (Figure 3c,d). Figure 3e–g show the front and side views of the RGO thermal probe in which we applied different driving currents of 200, 300, and 400 mA, respectively. This operation has also been recorded in Video S1 (Supporting Information) to show how the brightness of the thermal probe changes with the input power. The increased brightness of the probe with increasing input current indicates increasing temperature, as we characterize later. Similar to the tip feature probe, the RGO filament feature probes can also be triggered by electrical Joule heating to function as high–temperature thermal source (Figure 3h–j and Video S2: Supporting Information).

To reveal the effect of high-temperature Joule heating on the structure and electrical conductivity of the RGO probe, we characterized the change of RGO material before and after the electrical Joule heating process. After applying steady electrical Joule heating at a driving current of 400 mA (≈2400 K), the RGO probe exhibited a notable increase of conductivity (red curve in Figure 3k) due to the reduction and graphitization of RGO at the high temperature.[14] Structurally, as shown Figure 3I, after Joule heating the RGO probe exhibited a high-intensity graphitic (I_G) band and low-intensity disordered (I_D) band compared with the as-printed RGO probe, which indicates a high degree of graphitic structure after Joule heating.[15] The I_D/I_G ratio decreased from 0.95 in the as-printed RGO probe to 0.3 in the Joule-heating-reduced RGO probe, indicating that the number of defects in the reduced RGO probe significantly decreased. In addition, in our previous work, it has been demonstrated that the C/O atomic ratio significantly increases from 7.84 in the 1000-K-reduced RGO film to 130.6 in the 3000-K-reduced RGO film.[14] We also employed X-ray diffraction (XRD) to investigate the crystalline structures (Figure 3m), which shows the Joule-heating-treated RGO thermal probe exhibits a sharp peak at ≈26.316°, while the as-printed RGO probe shows a relatively broad peak at ≈23.158°, confirming the high graphitic crystallinity induced by the high-temperature Joule heating.

Thermogravimetric (TG) analysis (Figure S6, Supporting Information) reveals that F127 will be thermally decomposed/carbonized when heated to ≈650–700 K in nitrogen atmosphere during the pre-annealing process, which will not affect the structural stability of the RGO probe that is mainly composed of cross-linked graphene flakes. Comparing among the SEM images before (Figure 2h,i) and after Joule heating (Figure S7, Supporting Information), it was found that the probe after Joule heating features a cellular microstructure similar to that of probe before Joule heating, which indicates that Joule heating has no significant effect on its microstructure. The pre-annealing and Joule heating treatments greatly reduces
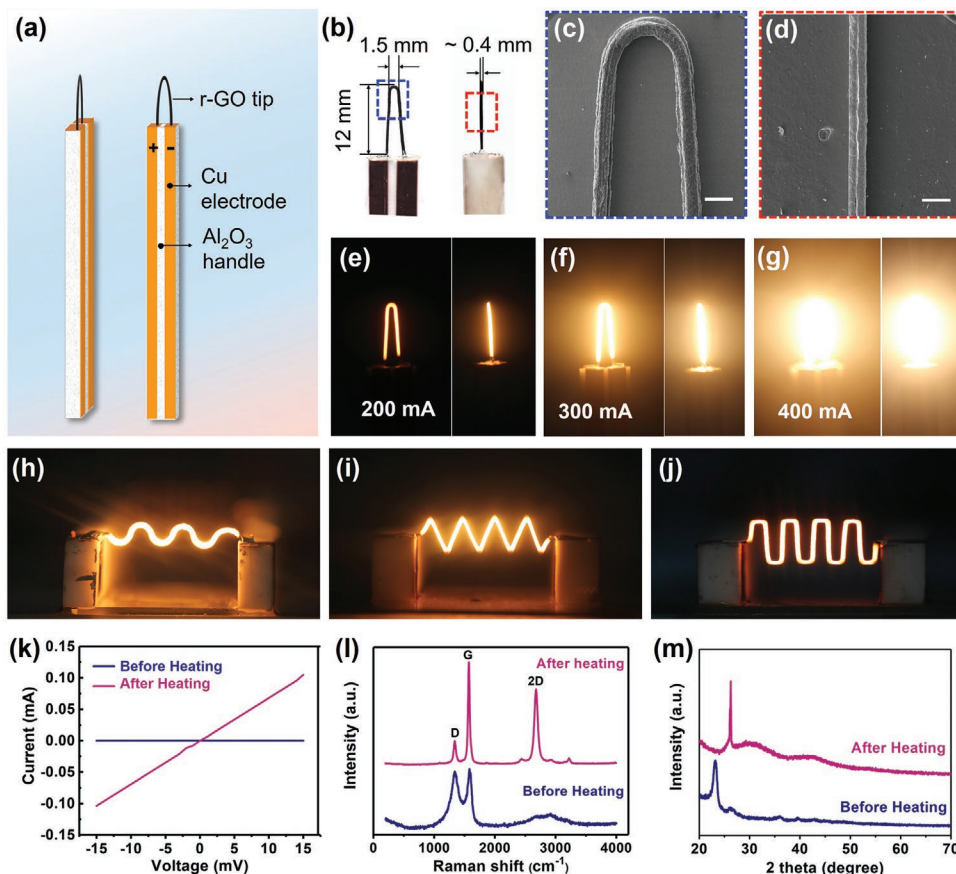
ADVANCED
SCIENCE NEWS
www.advancedsciencenews.com

ADVANCED
FUNCTIONAL
MATERIALS
www.afm-journal.de

Figure 3. High-temperature RGO thermal probes triggered by electrical Joule heating. a) Schematic diagram of the side (left) and front (right) views of the RGO thermal probe on an alumina ceramic handle attached to copper electrodes. b) Optical images of the front (left) and side (right) views of the RGO thermal probe with a narrow tip width (1.5 mm), a thin filament thickness of ≈400 μm, and a height of 12 mm. The size and shape of the RGO thermal probe can be easily adjusted by the printing program and nozzle diameter. c,d) The front and side view SEM images of the RGO probe. Scale bar is 500 μm. e–g) Front and side images of the RGO thermal probe under high temperature operations at input currents of 200, 300, and 400 mA, respectively. Optical images of the operation of with h) S–, i) saw–toothed– and j) right–angle–shaped RGO filament feature probes triggered by the applying current of 300 mA. k) The voltage as a function of the driving current for the RGO thermal probe before and after the Joule heating treatment. l) Raman spectra and m) XRD patterns of the RGO thermal probe before and after high-temperature Joule heating treatment.

and graphitizes the RGO probe and ensures its stable high-temperature Joule heating performance. Different with metals such as tungsten and tantalum, carbon material has a higher melting point and sublimation point (3915 K) in vacuum due to the strong C−C bond,[6a] which is important for the heating/synthesis operations under vacuum. To avoid the use of glovebox, we also explored placing the RGO probe in a plastic hose with a certain flow of argon gas to initially enable Joule-heating operation outside the glove box (Figure S8, Supporting Information) for a short time (≈30 s). Nevertheless, to realize the use of RGO probes in air ambient, further modifications are needed in future work.

To investigate the high-temperature heating performances of the RGO thermal probe, we measured its temperatures under different driving currents. Prior to the temperature measurement, we applied a steady Joule heating to the pre-annealed RGO probe at a driving current of 400 mA (≈7.4 W) to further reduce the RGO probe and stabilize its resistance. The temperatures of the RGO probes were calculated according to the color ratio pyrometry recorded by a high-speed camera that is

sensitive to the visible light spectrum (see Methods for more details). **Figure 4**a schematically shows how we monitored the temperature of the RGO thermal probe by a high-speed camera. A slow-motion video of the high-temperature RGO thermal probe driven by a current of 500 mA was recorded at 5000 frames pre-second (fps) (Video S3, Supporting Information). The current-time response curve (Figure S9, Supporting Information) with a current pulse of 1 millisecond shows that the RGO has the capability to achieve a high temporal resolution down to 1 millisecond. However, a short ramp-up time is still required to heat the RGO probe from room temperature to ultra-high temperatures (≈3000 K) by Joule heating. The calculated temperatures (Figure 4b, red curve) shows that the RGO probe can be turned on and reach ≈2740 K from room temperature in ≈7 milliseconds after the power was supplied, and turned off from ≈2900 K to produce no emission in less than 10 ms, exhibiting extreme heating and cooling ramping rates on the order of 10^5 K s^{-1} and therefore a high temporal resolution (milliseconds). The emission plot over time in Figure 4b (blue curve) is the intensity of visible light emitted by the RGO
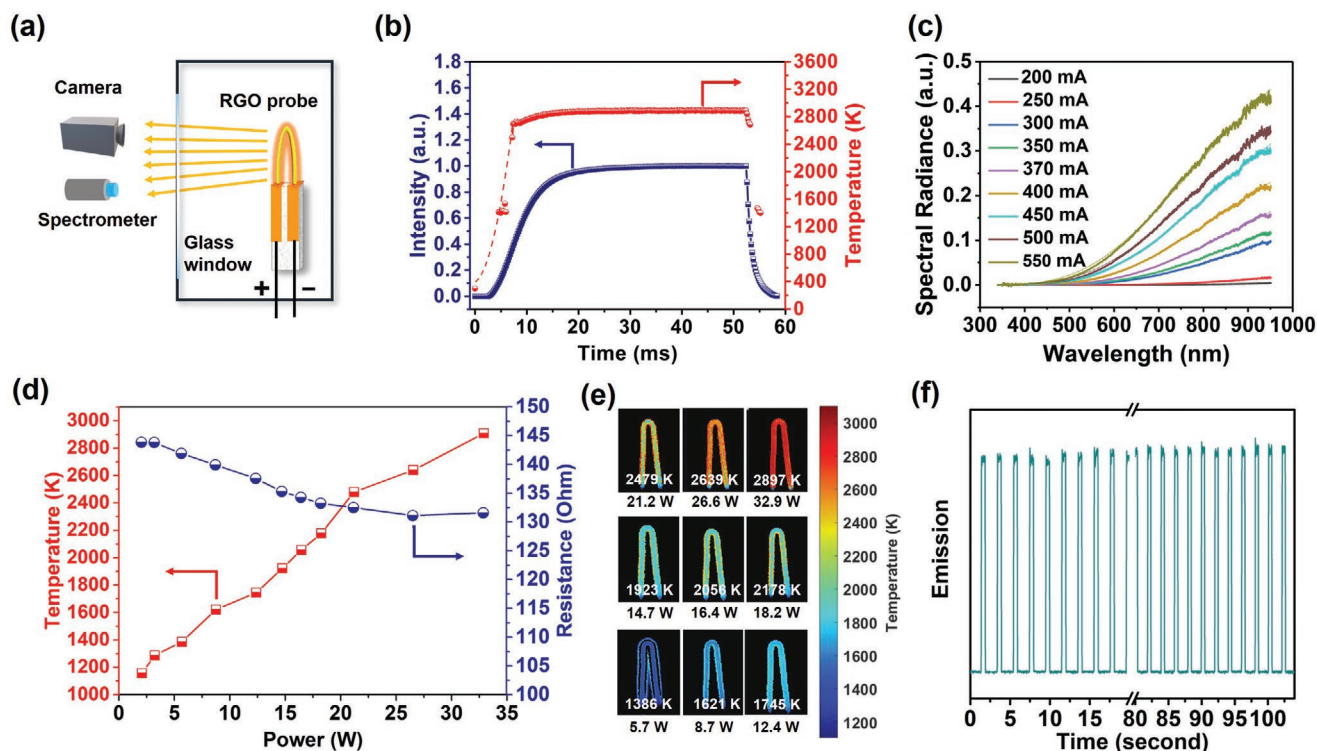
Figure 4. High temperature heating performance of RGO probe under Joule heating. a) Schematic diagram of the operation of RGO probe in the glove-box with argon atmosphere and temperature monitoring by a high-speed camera and spectrometer. b) The temporal evolution of emission and temperature during the rapid Joule-heating process. c) The emission spectra of an RGO probe Joule-heated under different input powers. d) The temperatures of the electrical Joule-heated RGO thermal probe as a function of the input power. e) Images recorded by the high-speed camera of the RGO probe under different input powers. f) The RGO probe can be stably turned on and off without degradation.

probe recorded by a Vision Research Phantom Miro M110 high-speed camera. This curve is simply estimated by summing all of the pixel light intensity values frame-by-frame in a video and then normalizing the values by the summed light intensity in the brightest frame.

Figure 4c reveals that the intensity of the radiation spectra of the RGO probe increases with the increasing current applied (i.e., power). The calculated mean temperature and the resistance of the RGO probe as a function of the input power are summarized in Figure 4d. The images of the RGO thermal probe recorded by the high-speed camera at different driving input currents are also presented in Figure 4e. The calculated mean temperature of the probe is ≈2897 K when the input current is 500 mA, and the maximum temperature is higher than 3000 K. Importantly, the temperature nearly linearly increases with the input power, which allowed us to easily adjust the working temperature of the RGO thermal probe. We believe the near-linear relationship between the temperature and power in the low input power range (0.65–20.48 W) is due to the principle of Joule-heating and the stable resistance of the RGO derived from pre-annealing. Therefore, although the high-temperature generated by the subsequent Joule heating will further reduce the RGO and improve its graphitization level, the decrease in resistance is relatively negligible. In addition, the cellular microstructure of the RGO sheets has few internal contacts inside the RGO probe and therefore a larger contact resistance, which also allows the RGO to maintain a relatively

high resistance after the high-temperature Joule heating, facilitating high-temperature Joule heating at low input currents.

As the input power increases to over 20.48 W, high-temperature thermal emission becomes important. The slope of temperature-power curve decreases accordingly and slightly deviates from the linear relationship. The emission intensity of the RGO probe at a fixed input current (500 mA) (Figure 4f) shows that the RGO can be turned on and off and maintains a constant emission intensity. In principle, light intensity of an emitting body scales with temperature and therefore one could think of the light intensities as analogues of temperature profiles. The stable emission intensity is therefore indicative of the good high-temperature stability of the RGO probe. The flickering of RGO thermal probe (Video S4, Supporting Information) by inputting a pulsed current also indicates the excellent pulse thermal heating capability and good stability of the probe.

As characterized above, this high-temperature RGO thermal probe has the following distinct advantages over traditional heating techniques: 1) a flexible heating-probe shape design with a microscale tip feature made possible by 3D printing; 2) highly controllable and stable heating (extreme temperature, ultrafast ramping rates) with a high temporal resolution (milliseconds) made possible by electrical Joule heating. These features make the RGO thermal probe an ideal heating source for materials synthesis and manufacturing, such as patterning of metal nanoparticles (NPs) which requires both spatial and temporal control over the heating process. As a proof of concept,
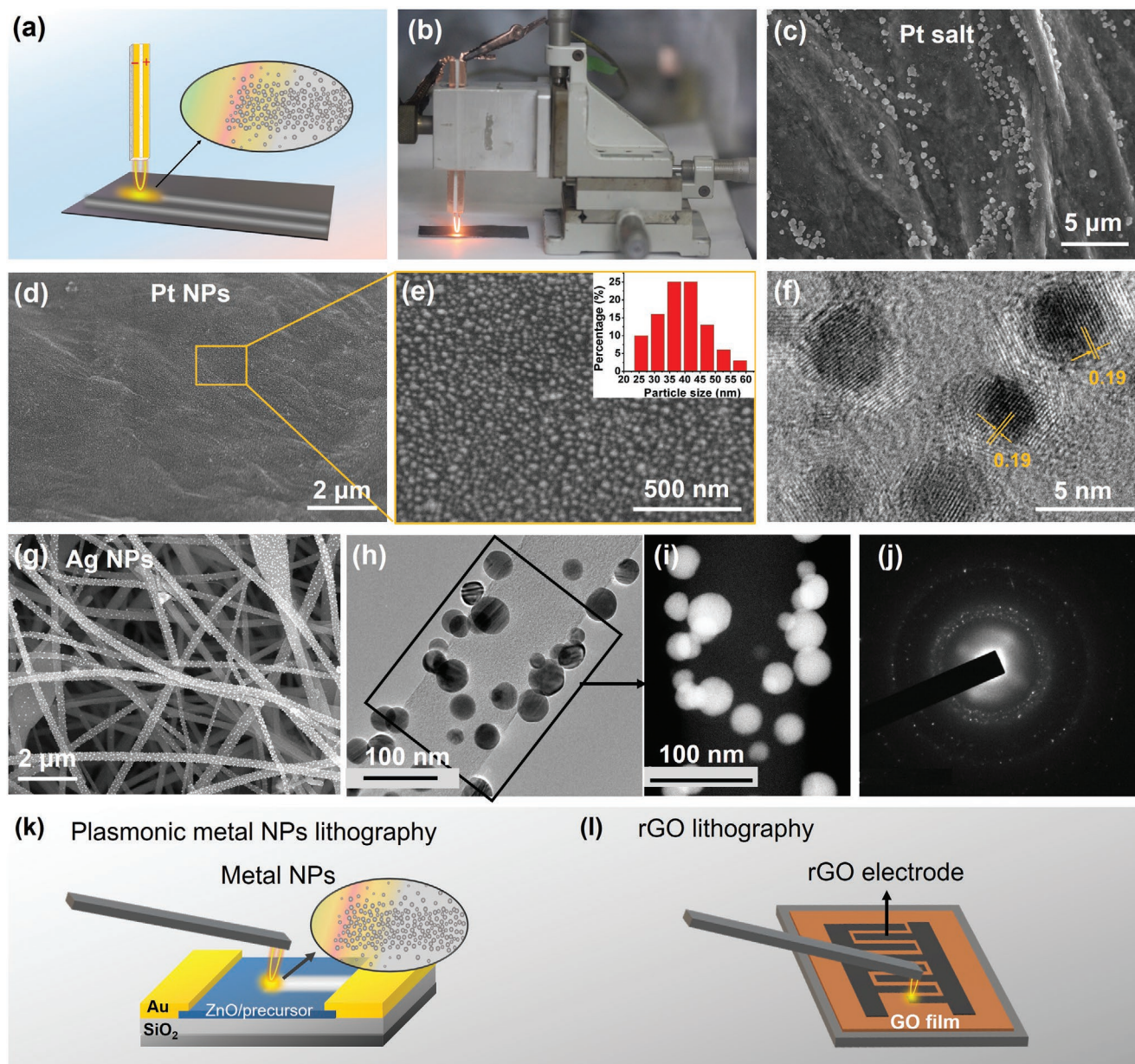
Figure 5. Synthesis of Pt and Ag nanoparticles by the RGO thermal probe. a) Schematic demonstration of the thermal patterning of metal NPs on the surface of a nano-carbon substrate through a rapid radiative heating process by the high-temperature RGO thermal probe. b) Optical image of the setup and its operation for the fabrication of Pt NPs on an RGO film using the high-temperature thermal probe triggered by electrical Joule heating. c) SEM image of the platinum chloride precursor aggregates deposited on the RGO film. d,e) SEM images of Pt NPs on the RGO film after the high-temperature synthesis. Inset is the size distribution histogram of the Pt NPs on the RGO surface. f) The high-resolution TEM image of the Pt NPs indicating the lattice spacing is 0.19 nm, which corresponds to the (200) crystalline plane. g–i) SEM and TEM images of the Ag NPs synthesized on CNFs. j) SAED pattern of the Ag NPs. Scalebar in the inset is 500 nm. k–i) Schematic of RGO probe-based thermal scanning lithography for the fabrication of a plasmon field-effect transistor k), and the selective reduction of GO to interdigitated RGO electrodes l).

we used an RGO probe device to perform the thermal shock synthesis of Pt and Ag NPs on nano-carbon substrates by rapidly heating and quenching the substrates pre-loaded with metal salt precursors (**Figure 5**a). Nano-carbons were chosen as the substrate because the metal nanoparticles hosted in carbon matrices are ubiquitous for various applications, such as (electro-) catalysis and energy storage.[16] To precisely control the position and movement of the RGO thermal probe, we fixed

the alumina ceramic handle of the device on a 3D motion platform, as shown in Figure 5b. RGO films with smooth surface morphology (Figure S10a,b: Supporting Information) are used as substrates. The carbon nanofiber (CNF) films (Figure S10c,d: Supporting Information) were also used as substrate to verify the compatibility of this method with substrate surface morphology. Prior to the radiative heating thermal shock treatment by the high-temperature RGO thermal probe, we dipped the

ethanol solution of H_2PtCl_6 (0.05 mol L^{-1}) onto RGO film as a Pt precursor, with a loading of $\approx 5 \times 10^{-6}$ mol cm^{-2} (Figure 5c). In a typical radiative heating thermal shock treatment process, the high temperature thermal probe was swept across the surface of the H_2PtCl_6-decorated RGO film in an argon atmosphere.

Figure 5d,e reveals that in the area swept by the probe contained numerous Pt NPs uniformly dispersed on the surface of the RGO substrate. The size distribution histogram was further calculated from 100 Pt particles and presented in the inset in Figure 5e, showing an average size of 36 nm. A high-resolution TEM image (Figure 5f) further reveals the 0.19 nm lattice fringe spacing of the NPs, corresponding to the (200) crystalline plane of a face-centered cubic (fcc) platinum crystalline structure.[17] The synthesis of metal nanoparticles by the rapid thermal shock method includes the following two processes: 1) the thermal decomposition of metal salts under high-temperature and 2) the metal particles nucleation and growth.[1b,18] In the process, the high temperature drives the salt decomposition while the short radiative heating duration is critical to avoid coarsening and aggregation.[18a,19] In contrast, conversional heating method are difficult to have accurate temporal and spatial control, which often leads to NP agglomeration. Since this is a rapid and non-equilibrium synthesis process, the metal NPs often exhibit a spherical shape to minimize the surface energy. By adjusting the heating duration and/or the amount of loaded metal salts, the size and amount of metal NPs could be controlled. Furthermore, due to the precisely controlled temperature of the thermal probe, various metal NPs can be synthesized by adjusting the temperature higher than the decomposition temperatures of the corresponding salt precursors.[1b,18a]

To illustrate the universal applicability of this method in the synthesis and patterning of metal NPs, Ag NPs were also synthesized on a CNF film using $AgNO_3$ as the salt precursor. Figure 5g–i shows that Ag NPs with diameters ranging from $\approx 20–50$ nm were deposited on the CNF surfaces through a high-temperature thermal shock process. The multi-ringed selected area electron diffraction (SAED) pattern suggests that the Ag NPs are polycrystalline (Figure 5j). Similar to the tip feature probe, by placing the film preloaded with metal salt precursor close to the filament feature probes (Figure S11, Supporting Information), NPs could also be rapidly synthesis on substrate by adjusting the temperature and time of electrical Joule heating without moving the thermal source and the film. The distribution of the NPs synthesis using this method would consistent with the geometry of the RGO filaments, which is conducive to more convenient and rapid preparation of patterned NPs. As an example, by placing H_2PtCl_6-decorated CNF films close to the RGO filaments (Figure S11a, Supporting Information) and performing a pulsed electrical Joule heating (0.5 s), the Pt NPs were synthesized in the area close to the RGO filament feature probes (Figure S11b,c: Supporting Information).

The great tunability of the RGO probe allows for flexible control of the scanning path of the probe tip, which in turn allows us to precisely pattern metal NPs in selected areas on the substrate. As a proof-of-concept, we prepared a S-shaped Ag NPs pattern on the surface of CNF film (Figure S12, Supporting Information). This result indicates that it is feasible to use the RGO probe in a thermal scanning probe lithography approach for fast integrating metal NPs in a selected region, which potentially enables rapid construction of plasma-enhanced devices (Figure 5k). The patterning capability and resolution of NPs via this approach depends on the size of the probe, the distance between the probe tip and the substrate surface (Figure S13, Supporting Information), and the probe temperature. The probes with smaller sizes can naturally create finer patterns with higher resolution. Considering the scope of this work, detailed optimization and fine-tuning of the RGO probes and their combination with probe temperature, precursor loading, and radiation distance on the minimum patterning dimensions will be carried out in the future. Additionally, this facile and fast thermal patterning process also provides a potentially effective strategy for patterned reduction of GO film to RGO electrodes (Figure 5l) and materials cutting (Figure S14, Supporting Information). Therefore, by integrating 3D printing with electrical Joule heating, we have provided an effective strategy for high precision thermal-driven micro/nano-manufacturing with precise spatial and temporal resolution. Importantly, according to the heating requirement, the size and geometry of the RGO probe can be easily adjusted by changing the printing parameters, which provides great flexibility of heating operation and potentially expands its application.

3. Conclusion

In this work, we demonstrated that 3D printed RGO thermal probes triggered by electrical Joule heating can function as high-performance heating sources with high spatial and temporal resolutions for micro/nanoscale thermal patterning and nanomaterial synthesis. The good flexibility and controllability of the extrusion-based 3D printing strategy enables the size, shape, and geometry of the RGO thermal probe to be flexibly designed and tuned according to the heating requirements. The RGO thermal probe is thermally stable and can achieve temperatures of up to ≈ 3000 K, with an ultrafast heating/cooling rate and a high temporal resolution (milliseconds), enabling the extreme and non-equilibrium heating that is highly desirable for thermal patterning and nanomaterial synthesis. As a demonstration, we used the RGO thermal probe to pattern metal NPs (Pt and Ag) on nano-carbon substrates coated with metal salt precursors by precisely control the heating location and duration. Therefore, we provided an effective heating strategy for high precision thermal-driven surface pattern and micro/nano-manufacturing. We also anticipate this 3D printed thermal probe can be readily extended to a range of applications where precise heating (position and duration) is required.

Conflict of Interest

The authors declare no conflict of interest.

Author Contributions

Data Availability Statement

Keywords

[1] a) C. Wang, W. Ping, Q. Bai, H. Cui, R. Hensleigh, R. Wang, A. H. Brozena, Z. Xu, J. Dai, Y. Pei, C. Zheng, G. Pastel, J. Gao, X. Wang, H. Wang, J.-C. Zhao, B. Yang, X. Zheng, J. Luo, Y. Mo, B. Dunn, L. Hu, *Science* **2020**, *368*, 521; b) Y. Yao, Z. Huang, P. Xie, S. D. Lacey, R. J. Jacob, H. Xie, F. Chen, A. Nie, T. Pu, M. Rehwoldt, D. Yu, M. R. Zachariah, C. Wang, R. Shahbazian-Yassar, J. Li, L. Hu, *Science* **2018**, *359*, 1489; c) B. R. Golla, A. Mukhopadhyay, B. Basu, S. K. Thimmappa, *Prog. Mater. Sci.* **2020**, *111*, 100651; d) Y. Arai, R. Inoue, K. Goto, Y. Kogo, *Ceram. Int.* **2019**, *45*, 14481.

[2] a) J. Chen, Y. Sun, L. Zhong, W. Shao, J. Huang, F. Liang, Z. Cui, Z. Liang, L. Jiang, L. Chi, *Small* **2016**, *12*, 5818; b) R. Garcia, A. W. Knoll, E. Riedo, *Nat. Nanotechnol.* **2014**, *9*, 577; c) L. C. Teague, J. D. Batteas, *Adv. Eng. Mater.* **2005**, *7*, 811; d) D. Wouters, U. S. Schubert, *Angew. Chem., Int. Ed.* **2004**, *43*, 2480.

[3] a) S. Gottlieb, L. Lorenzoni, L. Evangelio, M. Fernández-Regúlez, Y. K. Ryu, C. Rawlings, M. Spieser, A. W. Knoll, F. Perez-Murano, *Nanotechnology* **2017**, *28*, 175301; b) M. Spieser, C. Rawlings, E. Lörtscher, U. Duerig, A. W. Knoll, *J. Appl. Phys.* **2017**, *121*, 174503; c) L. L. Cheong, P. Paul, F. Holzner, M. Despont, D. J. Coady, J. L. Hedrick, R. Allen, A. W. Knoll, U. Duerig, *Nano Lett.* **2013**, *13*, 4485; d) C.-M. Huang, C.-H. Yeh, L. Chen, D.-A. Huang, C. Kuo, *ACS Appl. Mater. Interfaces* **2013**, *5*, 120; e) H. F. Hamann, S. I. Woods, S. Sun, *Nano Lett.* **2003**, *3*, 1643; f) Y. K. Ryu Cho, C. D. Rawlings, H. Wolf, M. Spieser, S. Bisig, S. Reidt, M. Sousa, S. R. Khanal, T. D. B. Jacobs, A. W. Knoll, *ACS Nano* **2017**, *11*, 11890.

[4] a) R. D. Farahani, M. Dubé, D. Therriault, *Adv. Mater.* **2016**, *28*, 5794; b) J. A. Lewis, B. Y. Ahn, *Nature* **2015**, *518*, 42; c) H. Yuk, X. Zhao, *Adv. Mater.* **2018**, *30*, 1704028; d) Y. Jiang, Z. Xu, T. Huang, Y. Liu, F. Guo, J. Xi, W. Gao, C. Gao, *Adv. Funct. Mater.* **2018**, *28*, 1707024; e) X. Zhu, M. Liu, X. Qi, H. Li, Y.-F. Zhang, Z. Li, Z. Peng, J. Yang, L. Qian, Q. Xu, N. Gou, J. He, D. Li, H. Lan, *Adv. Mater.* **2021**, *n/a*, 2007772; f) Y.-F. Zhang, Z. Li, H. Li, H. Li, Y. Xiong, X. Zhu, H. Lan, Q. Ge, *ACS Appl. Mater. Interfaces* **2021**, https://doi.org/10.1021/acsami.1c03572; g) X. Zhu, Q. Xu, H. Li, M. Liu, Z. Li, K. Yang, J. Zhao, L. Qian, Z. Peng, G. Zhang, J. Yang, F. Wang, D. Li, H. Lan, *Adv. Mater.* **2019**, *31*, 1902479.

[5] a) K. Fu, Y. Wang, C. Yan, Y. Yao, Y. Chen, J. Dai, S. Lacey, Y. Wang, J. Wan, T. Li, Z. Wang, Y. Xu, L. Hu, *Adv. Mater.* **2016**, *28*, 2587; b) S. Naficy, R. Jalili, S. H. Aboutalebi, R. A. Gorkin III, K. Konstantinov, P. C. Innis, G. M. Spinks, P. Poulin, G. G. Wallace, *Mater. Horiz.* **2014**, *1*, 326; c) Q. Zhang, F. Zhang, S. P. Medarametla, H. Li, C. Zhou, D. Lin, *Small* **2016**, *12*, 1702.

[6] a) A. I. Savvatimskiy, *Carbon* **2005**, *43*, 1115; b) T. Li, A. D. Pickel, Y. Yao, Y. Chen, Y. Zeng, S. D. Lacey, Y. Li, Y. Wang, J. Dai, Y. Wang, B. Yang, M. S. Fuhrer, A. Marconnet, C. Dames, D. H. Drew, L. Hu, *Nat. Energy* **2018**, *3*, 148.

[7] a) M. Peng, Z. Wen, L. Xie, J. Cheng, Z. Jia, D. Shi, H. Zeng, B. Zhao, Z. Liang, T. Li, L. Jiang, *Adv. Mater.* **2019**, *31*, 1902930; b) Q. Zhang, F. Zhang, X. Xu, C. Zhou, D. Lin, *ACS Nano* **2018**, *12*, 1096.

[8] a) J. E. Smay, G. M. Gratson, R. F. Shepherd, J. Cesarano, J. A. Lewis, *Adv. Mater.* **2002**, *14*, 1279; b) Z. Liang, Y. Pei, C. Chen, B. Jiang, Y. Yao, H. Xie, M. Jiao, G. Chen, T. Li, B. Yang, L. Hu, *ACS Nano* **2019**, *13*, 12653.

[9] Z. Xu, H. Sun, X. Zhao, C. Gao, *Adv. Mater.* **2013**, *25*, 188.

[10] L. Dong, J. Yang, M. Chhowalla, K. P. Loh, *Chem. Soc. Rev.* **2017**, *46*, 7306.

[11] a) C. Zhu, T. Liu, F. Qian, T. Y.-J. Han, E. B. Duoss, J. D. Kuntz, C. M. Spadaccini, M. A. Worsley, Y. Li, *Nano Lett.* **2016**, *16*, 3448; b) L. Qiu, J. Z. Liu, S. L. Y. Chang, Y. Wu, D. Li, *Nat. Commun.* **2012**, *3*, 1241; c) L. Qiu, B. Huang, Z. He, Y. Wang, Z. Tian, J. Z. Liu, K. Wang, J. Song, T. R. Gengenbach, D. Li, *Adv. Mater.* **2017**, *29*, 1701553.

[12] a) Q. Fu, E. Saiz, A. P. Tomsia, *Acta Biomater.* **2011**, *7*, 3547; b) S. Tanaka, N. Nishiyama, Y. Egashira, K. Ueyama, *Chem. Commun.* **2005**, *16*, 2125.

[13] a) M. Yang, N. Zhao, Y. Cui, W. Gao, Q. Zhao, C. Gao, H. Bai, T. Xie, *ACS Nano* **2017**, *11*, 6817; b) Y. Shao, M. F. El-Kady, C.-W. Lin, G. Zhu, K. L. Marsh, J. Y. Hwang, Q. Zhang, Y. Li, H. Wang, R. B. Kaner, *Adv. Mater.* **2016**, *28*, 6719.

[14] Y. Wang, Y. Chen, S. D. Lacey, L. Xu, H. Xie, T. Li, V. A. Danner, L. Hu, *Mater. Today* **2018**, *21*, 186.

[15] a) A. C. Ferrari, D. M. Basko, *Nat. Nanotechnol.* **2013**, *8*, 235; b) M. S. Dresselhaus, A. Jorio, A. Hofmann, G. Dresselhaus, R. Saito, *Nano Lett.* **2010**, *10*, 751.

[16] a) A. B. Dongil, L. Pastor-Pérez, J. L. G. Fierro, N. Escalona, A. Sepúlveda-Escribano, *Catal. Commun.* **2016**, *75*, 55; b) C.-H. Liu, R.-H. Liu, Q.-J. Sun, J.-B. Chang, X. Gao, Y. Liu, S.-T. Lee, Z.-H. Kang, S.-D. Wang, *Nanoscale* **2015**, *7*, 6356; c) P. Avouris, C. Dimitrakopoulos, *Mater. Today* **2012**, *15*, 86; d) C. Tan, X. Huang, H. Zhang, *Mater. Today* **2013**, *16*, 29; e) J. Liu, Q. Ma, Z. Huang, G. Liu, H. Zhang, *Adv. Mater.* **2019**, *31*, 1800696.

[17] a) S. Pandey, S. B. Mishra, *Carbohydr. Polym.* **2014**, *113*, 525; b) Z.-Y. Zhou, X. Kang, Y. Song, S. Chen, *Chem. Commun.* **2012**, *48*, 3391.

[18] a) M. Jiao, Y. Yao, G. Pastel, T. Li, Z. Liang, H. Xie, W. Kong, B. Liu, J. Song, L. Hu, *Nanoscale* **2019**, *11*, 6174; b) X. Wang, Z. Huang, Y. Yao, H. Qiao, G. Zhong, Y. Pei, C. Zheng, D. Kline, Q. Xia, Z. Lin, J. Dai, M. R. Zachariah, B. Yang, R. Shahbazian-Yassar, L. Hu, *Mater. Today* **2020**, *35*, 106.

[19] Y. Chen, Y. Li, Y. Wang, K. Fu, V. A. Danner, J. Dai, S. D. Lacey, Y. Yao, L. Hu, *Nano Lett.* **2016**, *16*, 5553.